Journal of *Marine Science and Engineering*

MDPI

Article

Hydrodynamic Shape Design and Self-Propulsion Analysis of a Hybrid-Driven AUG

Chen-Wei Chen *, Zhao-Ye Zhou, Xu-Peng Chen and Xiao-Jing Zhou

Ocean College, Zhejiang University, Zhoushan 316021, China
* Correspondence: cwchen@zju.edu.cn

Abstract: Due to the lack of a powerful propulsion device in conventional autonomous underwater gliders (AUGs), their mobility and flexibility are insufficient, thus not being capable of also ensuring the stability of the motion route. Thus, it is necessary to further develop hybrid-driven AUGs. This paper applied CFD simulation and experimental analysis methods to study and design a hybrid-driven AUG with a propeller optimized from a type of AUG with swept-forward and swept-back wings. Through parameter adjustment, the hydrodynamic configuration was optimized, and the optimal hull design and hydrofoil type selection were proposed. The lift–drag ratio could be improved by up to 22.5% at an angle of attack of 8 degrees. The optimized AUG was combined with a single propeller for self-propulsion simulation. Aiming at the problem caused by the propeller torque on the AUG, the strategy of a contra-rotating propeller (CRP) was conducted to self-eliminate the propeller torque. The simulation results show that in the self-propulsion state, the torque of the contra-rotating propeller could be reduced by more than 92% compared with that of a single propeller, greatly reducing the impact on the hybrid-driven AUG and raising the navigation stability.

Keywords: hybrid-driven autonomous underwater glider (AUG); computational fluid dynamics (CFD); experimental fluid dynamics (EFD); hydrodynamic performance; self-propulsion simulation

Citation: Chen, C.-W.; Zhou, Z.-Y.; Chen, X.-P.; Zhou, X.-J. Hydrodynamic Shape Design and Self-Propulsion Analysis of a Hybrid-Driven AUG. *J. Mar. Sci. Eng.* **2023**, *11*, 886. https://doi.org/10.3390/jmse11040886

Academic Editor: Gregory Grigoropoulos

Received: 3 April 2023
Revised: 17 April 2023
Accepted: 20 April 2023
Published: 21 April 2023

1. Introduction

Marine economy and technology are playing an increasingly important role in improving the competitiveness of countries and regions. The prerequisite technology for the development and utilization of marine resources is to have advanced marine monitoring technology and equipment. As an energy-saving type of underwater vehicle, autonomous underwater gliders (AUGs) rely on buoyancy engine and wing–body configurations to realize zigzag navigation in the vertical plane during operation in a gliding motion, which has the advantages of low power consumption, low cost, and a wide range of operation in endurance [1–4], and is capable of ensuring the reliability of high space–time density detection and measurement of the ocean [5]. At the initial stage of diving, the buoyancy engine reduces its own displacement volume to make the gravity greater than the buoyancy and start diving. After reaching the target depth, under the action of the buoyancy engine, the displacement volume is changed, so that the buoyancy is greater than the gravity, thus realizing the transition from diving to floating-up. During the gliding process, the attitude of the glider can be controlled by adjusting the internal eccentric weight to move forth and back or rotate left and right along the main axis of the glider.

The hydrodynamic configuration is the key point for the design of an AUG, especially in terms of the hydrofoil or the hull. Through the towing tank test and CFD numerical simulation, Ebata et al. [6] studied the influence of different airfoil section shapes and grazing angles on the hydrodynamic characteristics of an AUG mounted with hydrofoils at a low Reynolds number, proposed the testing scheme for the AUG model, and completed the optimal design of the hydrofoils. Singh et al. [7] studied the hydrodynamic performance of a series of laboratory AUGs and emphasized the necessity of analyzing the hydrofoil

performance, which is in favor of predicting the spiral path of an AUG based on the lift and drag coefficient of the hydrofoil. Chen et al. [8] put forward an AUG with a diamond-shaped hydrofoil configuration, and analyzed the lift–drag ratio of the AUG with different hydrofoil grazing angles in uniform and non-uniform flow, finding that the AUG had an excellent wing-hull efficiency following a higher lift–drag ratio whilst the hydrofoil grazing angle was 15°. Shashank et al. [9] assessed the influence of the hydrofoil position on the overall hydrodynamic performance of an AUG, noting that the deployment of the hydrofoil near the stern could improve the performance in a larger range of the angle of attack while not yielding over the stall angle. Consequently, the enhanced lift–drag ratio of the AUG wing configuration would be beneficial to promote the motion capacity.

AUGs generally adopt buoyancy regulation combined with hydrodynamic hydrofoils to generate thrust. Although it shows the advantages from the aspects of power consumption and working range, it also limits its own navigation speed and motion trajectory, weakening the motility, thus making it impossible to achieve multidirectional and proximity observation and the monitoring of specific objects. Due to the lack of strong power source, it is not conducive to maintaining a stable track in a strong current environment [10,11].

For the problems above-mentioned, the concept of a hybrid-driven AUG has been proposed by researchers, which is to add other powerful propulsion devices such as propellers and pumps to the conventional AUG, the earliest by Richard Blidberg in 2001 [12]. When the hybrid-driven AUG performs routine operations, the buoyancy engine is the only power source to achieve an underwater gliding motion. In contrast, if the hybrid-driven AUG receives the task of observing a specific target, the propulsion mode would automatically switch to the strong one, with the propellers or pumps generating thrust. Furthermore, when encountering obstacles from a strong current during regular gliding movements, it can also simultaneously turn on the strong power source to maintain the trajectory and guarantee the positioning accuracy.

In 2004, Princeton University and the Canadian Institute of Oceanography collectively designed a hybrid-driven AUG named the “Hybrid Glider”, following the “Folaga” hybrid-driven AUG handled by NATO in 2003 [13,14]. Later, Kyushu University and the Marine Geoscience and Technology Institute of Japan developed a spindle-shaped hybrid-driven AUG in 2006, optimizing the hydrodynamic configuration and notably increasing its navigation range [15,16]. In 2007, the Florida Institute of Technology innovatively designed a flat hybrid-driven AUG called an “AUV-Glider” with an open-frame design and multiple propulsion devices [17,18]. After a few years, Teledyne Webb Research Company unveiled a classic “Hybrid Slocum” hybrid-driven AUG in 2011, of which the working efficiency in the gliding mode was substantially equivalent to that in the propulsion mode [19]. In 2014, Tianjin University developed and designed the “Petrel II” hybrid-driven AUG [20].

Self-propulsion analysis is a requisite for underwater vehicles, showing similarities, to a certain extent, to a hybrid-driven AUG. Nathan et al. [21] applied the CFD technique to analyze the influence of various turbulence models on the propeller performance and carried out a self-propulsion prediction for DARPA SUBOFF, referring to the thrust identity method. Pareecha et al. [22] utilized CFX software with the SST k-ω model to simulate the self-propulsion motion of a group of multiple AUGs with different spacing and arrangement, stressing the importance of wake fraction and thrust reduction during the research. Zhang et al. [23] designed a propeller for a low-speed underwater vehicle by the means of self-propulsion simulation with the effective wake distribution obtained, which was verified by the lake test. Liu et al. [24] carried out a self-propulsion simulation and route test of a submersible, detecting the increasing hull resistance with the propeller rotation rate. Self-propulsion test and simulation can therefore be effectively carried out to verify the interaction between the AUG and the adaptive propeller.

Compared with ships, AUGs are smaller in size, and hence the displacement-induced restoring moment for roll is smaller. Consequently, whilst the AUG will match an adaptive propeller, it is necessary to balance the torque generated by the propeller to maintain the dynamic motion stability. Propellers with the opposite rotation direction can be combined

to offset the torque produced by each other, which are named as contra-rotating propellers (CRPs) [25–27].

Presently, there are many studies on CRP, mainly aiming at the hydrodynamic performance analysis; however, there have been a few studies on its application to underwater vehicles. Wang [28] applied the CFD method to study the open water performance of two groups of CRP, in which the apparently periodic unsteadiness of the thrust and the torque output were the focus of the research. Hu et al. [29] selected the large eddy simulation method coupled with overset mesh strategy to predict the tip vortex of CRP in terms of the evolution and interaction of the tip vortex. Paik et al. [30] combined numerical simulation with the SPIV test to measure the wake of CRP, and found that CRP showed a greater wake contraction than a single propeller. He et al. [31] carried out comparative research on the wake field between CRP and the single propeller, proving that most of the kinetic energy generated by the front propeller of CRP can be absorbed by the rear one.

It should be noted that in the effective wake, propeller-induced slipstream causes a variation in local water pressure reacting on the AUG stern surface and the appendages, leading to an augmentation in the resistance. An effective propeller wake distribution would be predictable in the self-propulsion simulations. In addition, a self-propulsion factor dependent on the AUG forward speeds will be definitely predicted in the CFD simulations including effective horse power and QPC (quasi-propulsive coefficient) composed of the propeller efficiency in open-water performance, relative rotative efficiency, and hull efficiency, etc.

The purpose of this paper was to match and analyze a hybrid-driven AUG including the process of the optimization design for the hydrodynamic shape of the AUG from the perspectives of the lift–drag ratio and the hydrodynamic performance as well as the self-propulsion assessment of the hybrid-driven AUG with both a single propeller and CRP. The simulation results of the formative self-propulsion factor of the hybrid-driven AUG will be presented progressively.

2. Numerical Method

2.1. Governing Equations

Applying the CFD technique, the core for the calculation of the hydrodynamic performance of hybrid-driven AUG is the accurate solution of the Navier–Stokes equation. The governing equation aims to describe the conserved motion of fluid including the continuity equation and the momentum conservation equation. The momentum conservation equation is the embodiment of Newton's second law of motion-force and acceleration in fluid mechanics in accordance with the law of mass conservation, as shown in Equation (1) [32]:

$$\frac{\partial(\rho u_i)}{\partial \tau} + \frac{\partial(\rho u_i u_j)}{\partial x_j} = \rho F_i - \frac{\partial P}{\partial x_i} + \frac{\partial}{\partial x_j}\left(\mu \frac{\partial u_i}{\partial x_j}\right) \tag{1}$$

where u_i and u_j (i, j = 1, 2, 3) are the velocity components of the particle in x_i and x_j directions respectively; P is the pressure; ρ is the fluid density; τ is the time; F_i is the mass force; μ is the dynamic viscosity coefficient.

For practical engineering problems, due to the complexity of flow, the Reynolds average Navier–Stokes (RANS) equation is generally used for the calculation. The principle of solving RANS equations is to replace the statistical mean value with the time-averaged value, which can effectively solve practical engineering problems. After the time homogenization of the above Equation (1), the RANS equation is obtained as [33]:

$$\frac{\partial(\rho \overline{u_i})}{\partial \tau} + \rho \overline{u_j} \frac{\partial \overline{u_i}}{\partial x_j} = \rho \overline{F_i} - \frac{\partial \overline{P}}{\partial x_i} + \frac{\partial}{\partial x_j}\left(\mu \frac{\partial \overline{u_i}}{\partial x_j} - \rho \overline{u_i' u_j'}\right) \tag{2}$$

where $\overline{u_i}$ and $\overline{u_j}$ (i, j = 1, 2, 3) are the time-averaged velocity components of a particle in the directions of x_i and x_j, respectively; u_i' is the turbulence pulsation velocity component

relative to the time-averaged velocity; $\overline{F}_i$ is the mass force component; $\overline{P}$ is the mean of the pressure; μ is the dynamic viscosity coefficient of the fluid; $\rho\overline{u_i'u_j'}$ is the time-averaged Reynolds stress; $\rho\overline{F}_i$ represents the mass force.

2.2. Turbulence Model

In order to solve the RANS equation, it is necessary to calculate the Reynolds stress, leaving the selection of the turbulence model for the RANS equation as crucial [34]. The Reynolds number of the AUG in this paper was around 2.0×10^6. Singh Y. et al. [7], Sun C. et al. [35], and Divsalar K [36] applied the SST k-ω turbulence model to numerically simulate the hydrodynamic performance of AUG (the Reynolds number was in the order of 10^5–10^6), and it was found that the error between the simulation value and the experimental value was small. Therefore, the SST k-ω turbulence model was adopted in this paper.

The SST k-ω turbulence model combines the standard turbulence k–ω model for the boundary layer and the k-ε turbulence model for far field, as shown in Equations (3) and (4) [37]:

$$\frac{\partial}{\partial\tau}(\rho k) + \frac{\partial}{\partial_{xj}}(\rho k u_i) = \frac{\partial}{\partial_{xj}}(\Gamma_k \frac{\partial_k}{\partial_{xj}}) + G_k - Y_k + S_k \tag{3}$$

$$\frac{\partial}{\partial\tau}(\rho\omega) + \frac{\partial}{\partial_{xj}}(\rho\omega u_i) = \frac{\partial}{\partial_{xj}}(\Gamma_\omega \frac{\partial_\omega}{\partial_{xj}}) + G_\omega - Y_\omega + S_\omega + D_\omega \tag{4}$$

where G_k is the turbulence kinetic energy; G_ω is the ω equation; Γ_k and Γ_ω represent the effective diffusion term of k and ω, respectively; Y_k and Y_ω represent the effective divergence term of k and ω, respectively; S_k and S_ω are defined by the user. The effective diffusion equations of the model are shown as Equations (5) and (6).

$$\Gamma_k = \mu + \frac{\mu_\tau}{\partial_k} \tag{5}$$

$$\Gamma_\omega = \mu + \frac{\mu_\tau}{\partial_\omega} \tag{6}$$

where ∂_k and ∂_ω represent the turbulent Prandtl number of k and ω, respectively; μ_τ is the turbulent viscosity coefficient.

2.3. Dimensionless Parameters for Simulation and Test of AUG

The force analysis was established on the vertical section of the model, as shown in Figure 1. F_D is the drag of AUG, F_L is the lift, M is the torque, F_G represents the gravity, F_B represents the buoyancy, α is the angle of attack, ϕ *is* the pitch angle, and γ is the glide angle. The drag coefficient C_D and the lift coefficient C_L of AUG are calculated according to Equations (7) and (8).

$$C_D = \frac{F_D}{\frac{1}{2}\rho V^2 \nabla^{\frac{2}{3}}} \tag{7}$$

$$C_L = \frac{F_L}{\frac{1}{2}\rho V^2 \nabla^{\frac{2}{3}}} \tag{8}$$

where ρ is the water density; V is the velocity of inflow; $\bigtriangledown$ is the displacement of AUG.

2.4. Dimensionless Parameters for Simulation and Test of Propeller

Assuming that the propeller diameter is D, the rotational speed is n, the advance speed is V_A, the propeller thrust is T, and the torque is Q. Then, the advance speed coefficient J, thrust coefficient K_T, and torque coefficient K_Q, propeller efficiency η_o in the open water condition are [38]:

$$J = \frac{V_A}{nD} \tag{9}$$

$$K_T = \frac{T}{\rho n^2 D^4} \tag{10}$$

$$K_Q = \frac{Q}{\rho n^2 D^5} \tag{11}$$

$$\eta_o = \frac{TV_A}{2\pi nQ} = \frac{K_T}{K_Q} \cdot \frac{J}{2\pi} \tag{12}$$

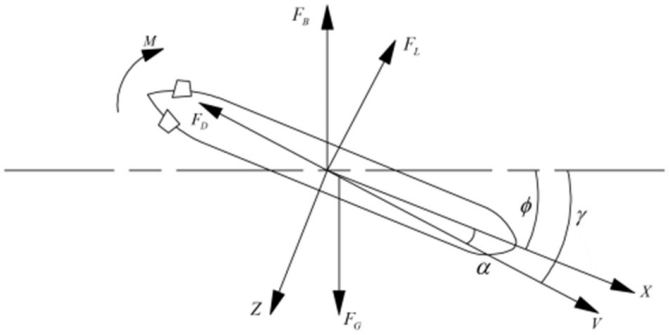

Figure 1. The force analysis of the AUG from the perspective of the vertical section.

The open water performance formula of CRP based on ITTC is shown in Equations (13) and (15) [39].

$$\text{Front propeller}: \begin{cases} K_{Tf} = \frac{T_f}{\rho n^2 {D_f}^4}, K_{Qf} = \frac{Q_f}{\rho n^2 {D_f}^5} \\ \eta_f = \frac{J}{2\pi} \cdot \frac{K_{Tf}}{K_{Qf}} \end{cases} \tag{13}$$

$$\text{Rear propeller}: \begin{cases} K_{Ta} = \frac{T_a}{\rho n^2 {D_a}^4}, K_{Qa} = \frac{Q_a}{\rho n^2 {D_a}^5} \\ \eta_a = \frac{J}{2\pi} \cdot \frac{K_{Ta}}{K_{Qa}} \end{cases} \tag{14}$$

$$\text{Contra} - \text{rotating propeller}: \begin{cases} T = \left|T_f\right| + |T_a| \\ Q = \left|Q_f\right| + |Q_a| \\ K_T = K_{Tf} + K_{Ta} \\ K_Q = K_{Qf} + K_{Qa} \end{cases} \tag{15}$$

2.5. Self-Propulsion Parameters of the AUG

Under the self-propulsion condition of the hybrid-driven AUG, the propulsion performance is related to power transmission and propulsion efficiency. The two most important horsepower are brake horsepower P_B and effective horsepower P_E, and the relationship between the two horsepower is shown in Equations (16) and (17).

$$P_E = P_B \cdot QPC \tag{16}$$

$$QPC = \eta_R \cdot \eta_o \cdot \eta_H \tag{17}$$

where QPC is the quasi-propulsive coefficient; η_R is the relative rotation efficiency; η_o is the open water efficiency of the propeller; η_H is the hull efficiency. The formula for each efficiency is calculated as in Equations (18)–(20).

$$\eta_R = \frac{Q_0}{Q_B} \tag{18}$$

$$\eta_o = \frac{T_B V_A}{2\pi n Q_0} \tag{19}$$

$$\eta_H = \frac{F_D V}{T V_A} \tag{20}$$

where T_B is the thrust of the propeller behind the hull; F_D is the drag of AUG; Q_0 is the torque of the propeller in the open water test; Q_B is the torque of the propeller under the self-propulsion condition; V is the navigation speed; V_A is the advance speed of the propeller.

3. Hydrodynamic Shape Optimization Design of the Hybrid-Driven AUG

This paper advanced the design of the hydrodynamic shape for AUG from two aspects, the hull line and the hydrofoil, mainly by numerical simulation with CFD software Star-CCM+, not taking the buoyancy and gravity of the AUG into account.

3.1. Main Dimension Parameters of the Hybrid-Driven AUG

This paper developed the hybrid-driven AUG based on the design of the AUG *Sea-wing* [40]. Its hydrofoil consists of a pair of forward-swept wings and a pair of backward-swept wings, and presents a rhomboid structure, as shown in Figure 2, considering the enhanced lift–drag ratio. This paper terms the hydrofoil configuration as a rhomboid wing for the convenience of expression. The main dimension parameters of the AUG are shown in Table 1 [8].

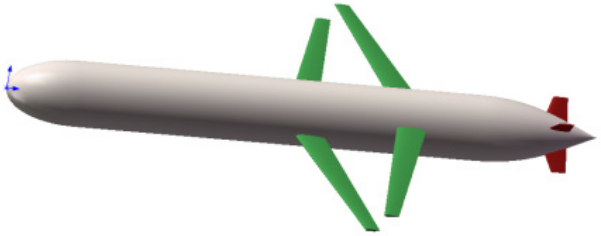

Figure 2. Concept model for the hydrodynamic shape based on the AUG *Sea-wing*.

Table 1. Main dimension parameters of the AUG.

Parameter	Symbol	Value	Unit
Effective maximum length	L	2.00	[m]
Maximum diameter of the hull	D_h	0.22	[m]
Length of the bow	L_1	0.23	[m]
Length of the stern	L_2	0.40	[m]
Wingspan of the hydrofoil	B	0.60	[m]
Chord length of the hydrofoil tip	C_t	0.05	[m]
Chord length of the hydrofoil root	C_r	0.10	[m]
Wet surface area of the hydrofoil	S	0.18	[m^2]
Displacement volume	∇	0.0646	[m^3]

3.2. Simulation Settings

3.2.1. Calculation Domain

The CFD calculation domain in this section was set for the simulations presented in Sections 3.2–3.4 according to the recommendations of the ITTC [41], which suggests that the inlet boundary should be located at a distance of L~2 L from the bow of the glider, and the outlet boundary should be located at a distance of 3 L~5 L from the stern. Accordingly, in this paper, the bow of the AUG was located at 2 L from the velocity inlet, and the stern was located at 5 L from the pressure outlet, as shown in Figure 3.

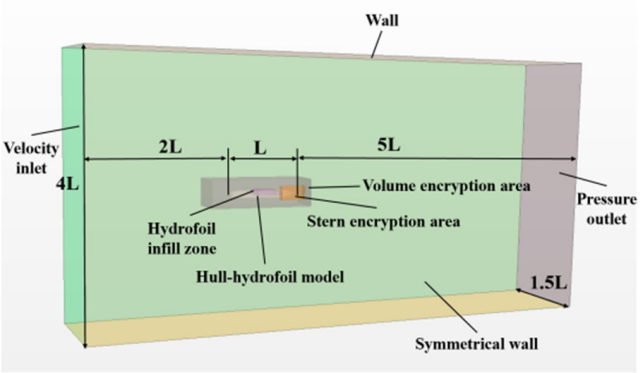

Figure 3. Numerical tank with the boundary conditions.

3.2.2. Mesh Strategy

In order to better capture the flow field around the hydrofoil, an encryption area was established around the hydrofoil together with the vicinity of the bow, the stern, and the rudders being encrypted. In order to more accurately capture the flow details near the wall, five layers of prismatic mesh were set along the normal direction of the wall, with the total thickness of 0.01 m. The mesh result is shown in Figure 4.

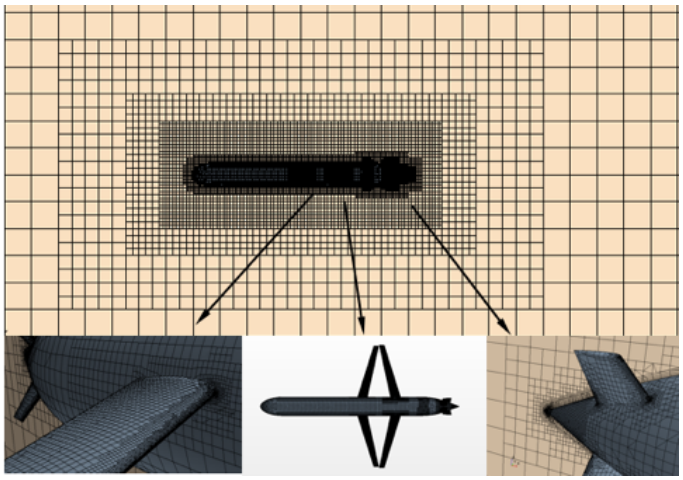

Figure 4. Mesh of the AUG.

3.2.3. Mesh Independence Analysis

By changing the basic mesh size (0.50 m, 0.25 m, 0.20 m, 0.15 m, respectively) to set a different total cell number, a mesh independence analysis was conducted for the hybrid-driven AUG without the propeller, with the time step set as 0.001 s and the uniform inlet velocity set as 1.0 m/s, as shown in Figure 5. It shows that when the total number of grids increased to more than 2.1×10^6, the drag value basically remained stable. Considering the calculation accuracy and the time cost, this mesh setting was selected to calculate the hydrodynamic performance of the AUG in this paper.

The mesh quality was assessed using the volume change metric to describe the ratio of the cell volume to the largest adjacent cell volume according to the user guide for Star-CCM+ [42]. When the volume jump between two mesh cells becomes excessively large, it may cause imprecise and unstable solvers. A volume change of 1.0 indicates a cell volume greater than or equal to its adjacent cells; cells with a volume change equal to or less than 0.01 are considered as bad mesh cells.

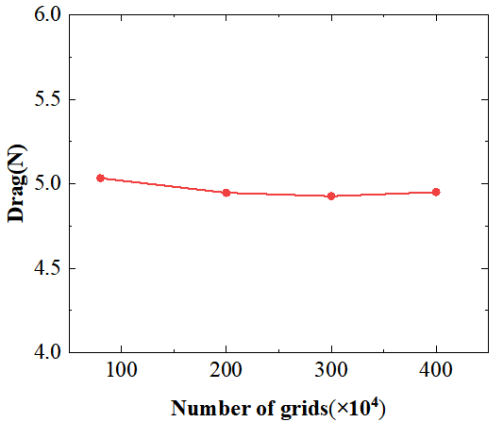

Figure 5. Mesh independence of the AUG in terms of drag.

The distribution of the volume change and y^+ within the calculation domain is shown in Figure 6. The majority of the cell volume changed between 0.1 and 1.0; there was no cell with a volume change less than 0.01, indicating that the mesh quality is reliable.

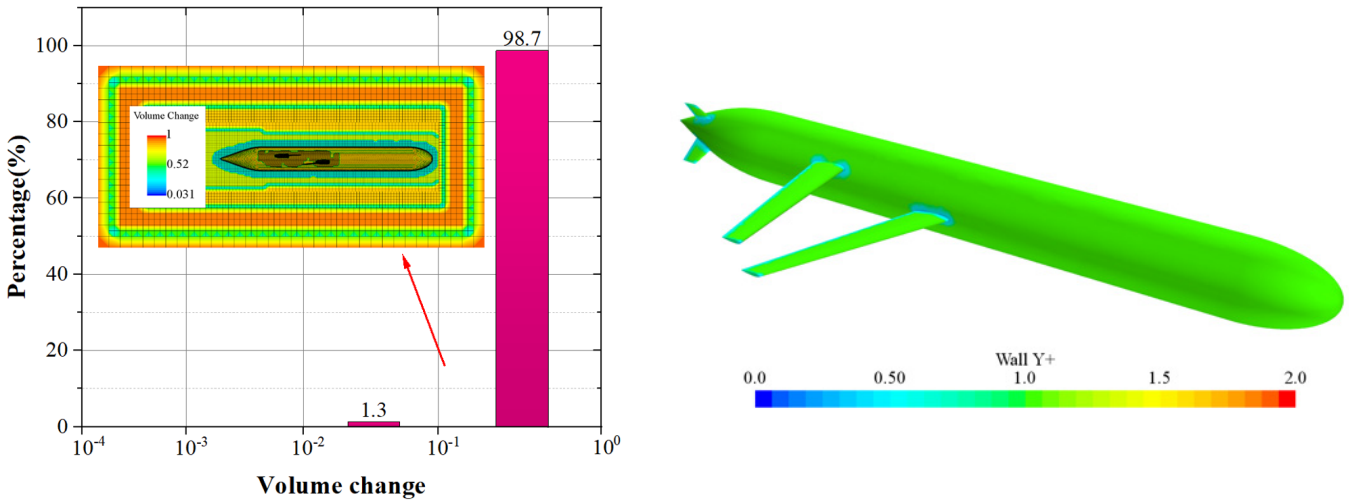

Figure 6. Mesh quality evaluation by the volume change method (**a**) and y+ distribution (**b**) (mesh base size 0.25 m).

3.3. Type Selection Design for Hull Line

Myring streamline was applied to design the hull line composed of a bow curve and stern curve. The bow curve in the longitudinal section is ellipse, and the stern curve is a polynomial curve determined by the angle of the run [43]. Equations (21) and (22) are the curve expressions, and the origin of the coordinate is set at the center point of the bow end.

Bow curve:

$$r(x) = \frac{1}{2}D_h\left[1 - \left(\frac{x-a}{a}\right)^2\right]^{\frac{1}{p}} \tag{21}$$

Stern curve:

$$r(x) = \frac{1}{2}D_h - \left(\frac{3D_h}{2c^2} - \frac{\tan\theta}{c}\right)(x-a-b)^2 + \left(\frac{D_h}{c^3} - \frac{\tan\theta}{c^2}\right)(x-a-b)^3 \tag{22}$$

where a represents the length of the bow; b is the length of the parallel middle body; c is the length of the stern; D is the diameter of the parallel middle body; p is the sharpness factor; θ is the angle of run. In the models, a = 0.230 m, b = 1.370 m, and c = 0.400 m.

A total of 12 kinds of axisymmetric hull models in terms of the combination of the bow and stern line parameters were constructed (p = 2,3,4; θ = 15°, 25°, 35°, 40°). Figure 7 lists the hull models with different values of p and θ (p = 2; θ = 25°), (p = 4; θ = 40°).

(**a**) (**b**)

Figure 7. Three-dimensional sketch of two kinds of hull models, the model with p = 2; θ = 25° (**a**) and the model with p = 4; θ = 40° (**b**).

The simulations of the 12 hull models were carried out at the same speed of V = 1.0 m/s. Figure 8 shows the simulation results of the drag coefficient for different hull models.

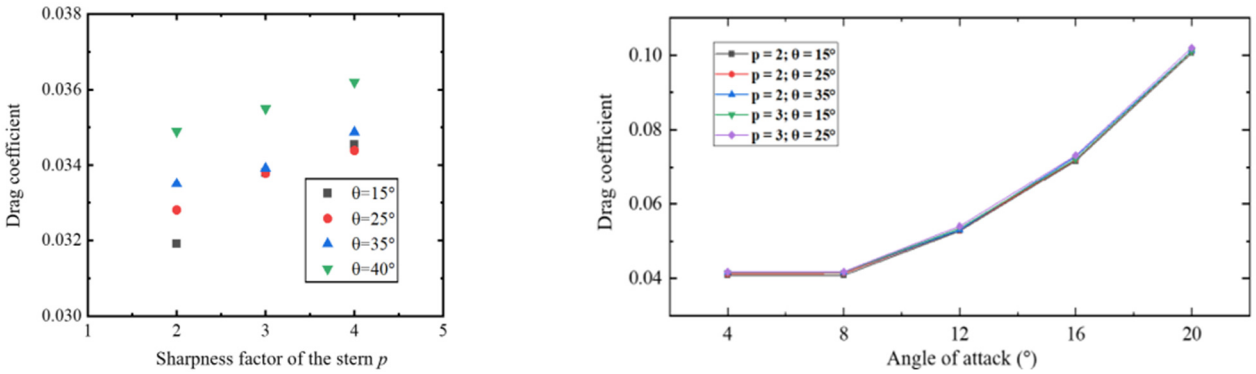

(**a**) (**b**)

Figure 8. Drag coefficient of different hull models in terms of straight-line motion (**a**) and oblique motion (**b**) with different angles of attack.

It can be seen that if the angle of run θ was the same (i.e., the stern profile line is the same), with the increase in the bow sharpness factor p value (i.e., the fuller the bow curve), the drag coefficient basically showed a trend of gradual increase. Under the same sharpness factor p value, the hull drag coefficient was the largest when θ was 40°.

Under the same sharpness factor p = 3 or p = 4, the drag coefficient values of θ at 15°, 25°, and 35° showed little difference, which indicates that the effect of the stern angle of run θ on the overall drag coefficient was minor when the bow was relatively full. However, when the sharpness factor p was 2, the plumpness of the bow curve was relatively low, and the effect of θ on the overall drag coefficient was greater.

As far as the drag coefficient is concerned, the drag reduction performance was better when the profile p was 2. The drag coefficient of the hull increased with the rise in the angle of attack, and the growth rate of the drag coefficient increased gradually. Consequently, the models of (p = 2; θ = 15°) and (p = 2; θ = 25°) showed a relatively nice drag reduction performance.

The calculation results of the initial hull model show that the drag coefficient of straight-line motion is 0.0329, while the drag coefficient of the model with the profile line (p = 2; θ = 15°) is 0.0319. The drag coefficient compared with the original model is reduced by 3.04% for the optimized model. Consequently, the hull line (p = 2; θ = 15°) was selected for the design.

3.4. Selection and Design of Hydrofoil Profile

Considering the need for the selection of rhomboid hydrofoils for the AUG, the following six types of airfoils were selected as the research object in this section including

symmetrical airfoils and asymmetric airfoils. Combined with the optimal hull described in Section 3.2, the hydrodynamic performance under variable angles of attack was analyzed. The geometrical profiles of the six airfoils are shown in Figure 9.

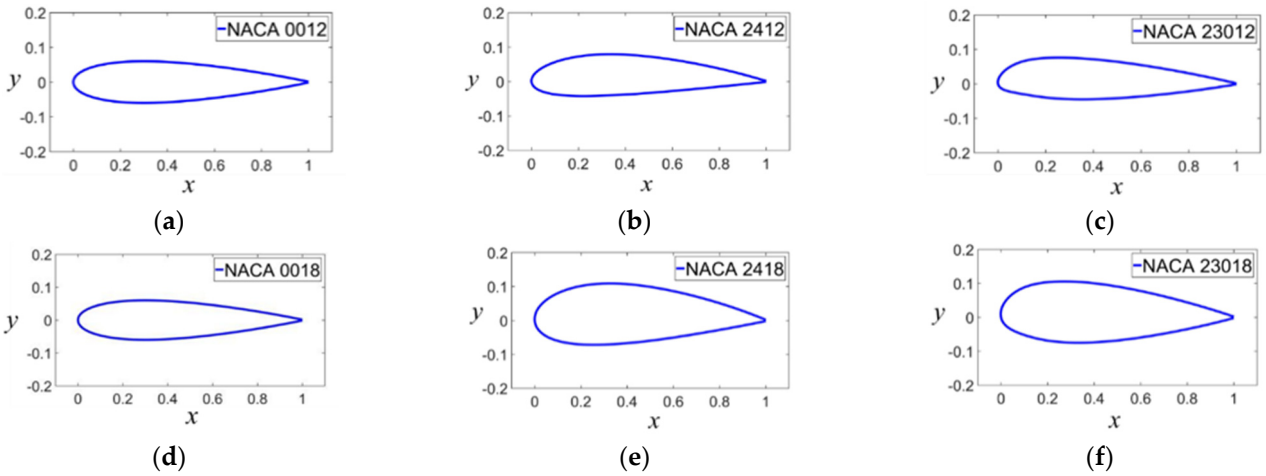

Figure 9. Geometric sketch of the six different airfoil profiles: NACA0012 (**a**), NACA2412 (**b**), NACA23012 (**c**), NACA0018 (**d**), NACA2418 (**e**), and NACA23018 (**f**).

The dimensionless hydrodynamic coefficients of the rhomboid wing of AUG at the angle of attack of $-4° \leq \alpha \leq 25°$ were respectively calculated when the inflow velocity was set as 1.0 m/s. Figure 10 shows the simulation results of the AUG lift coefficient, drag coefficient, and lift–drag ratio with different angles of attack.

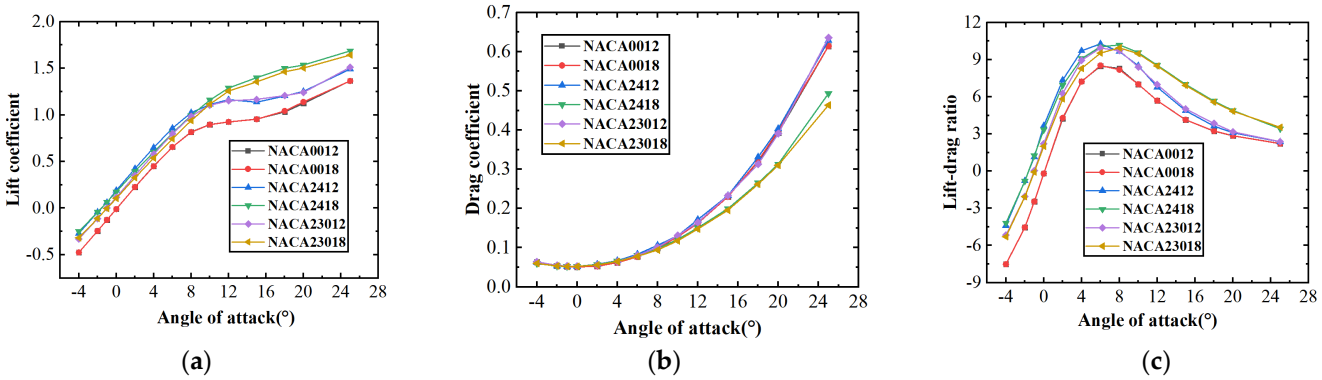

Figure 10. Hydrodynamic calculation results of the rhomboid wing with different types of airfoils, lift coefficient (**a**), drag coefficient (**b**), and lift–drag ratio (**c**).

The following can be obtained from Figure 10a. (1) When the angle of attack was $-4° \leq \alpha \leq 25°$, the lift coefficient increased gradually with the angle of attack, but the rate slowed down in the range of angle of attack α out of 10°. (2) The zero-lift angle of attack with symmetric airfoils (NACA0012 and NACA0018) appeared when $\alpha = 0°$, while the angle of attack of zero lift with asymmetric airfoil was in the range of $-2° \leq \alpha \leq 1°$. (3) The lift coefficients with airfoils NACA2418 and NACA23018 were slightly smaller than that with airfoils NACA2412 and NACA23012 in the range of $-4° \leq \alpha \leq 8°$ (small angle of attack), but showed the greatest value when $10° \leq \alpha \leq 25°$ (large angle of attack).

According to Figure 10b, the following were discovered. (1) The drag coefficient of the AUGs with different rhomboid hydrofoils increased with the growth in the angle of attack in the range of $0° \leq \alpha \leq 25°$ for the angle of attack, accelerating gradually. When the angle of attack was less than 6°, the difference was very small. (2) The drag coefficients of the AUGs with airfoils NACA2418 and NACA23018 were smaller.

Figure 10c shows the following. (1) The maximum lift–drag ratio of the AUGs with different rhomboid hydrofoils appeared when the angle of attack was $6° \leq \alpha \leq 8°$, and the ones with airfoils NACA2418 and NACA23018 behaved best. (2) The linear relationship between the lift–drag ratio and the angle of attack ended in the range of 5~8°. After that, the lift–drag ratio of each model began to show a downward trend due to the significantly stronger growth of the drag coefficient and the slower growth of the lift coefficient closely related to the headstream surface of the AUG. (3) In general, in the range of a small angle of attack ($-4° \leq \alpha \leq 8°$), the lift–drag ratio performance with airfoil NACA2412 was better, while in the range of a larger angle of attack ($10° \leq \alpha \leq 25°$), the performance with airfoil NACA2418 was more outstanding.

Through comprehensive consideration of the three factors above-mentioned, airfoil NACA2418 was selected for the design and analysis of the hybrid-driven AUG with rhomboid wings in this paper. In order to investigate the difference in the hydrodynamic performance of the AUGs with different hydrofoils and the interactive influence between the front and rear hydrofoils of the same airfoil at different angles of attack, the longitudinal profile of the hydrofoil in Figure 11 was selected to extract the velocity and streamline distribution, as shown in Figure 12.

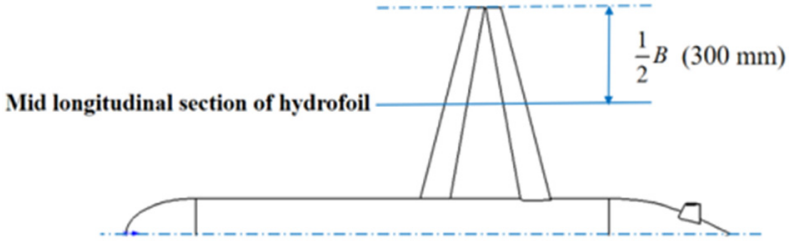

Figure 11. The hydrofoil profile in the longitudinal section in the center plane.

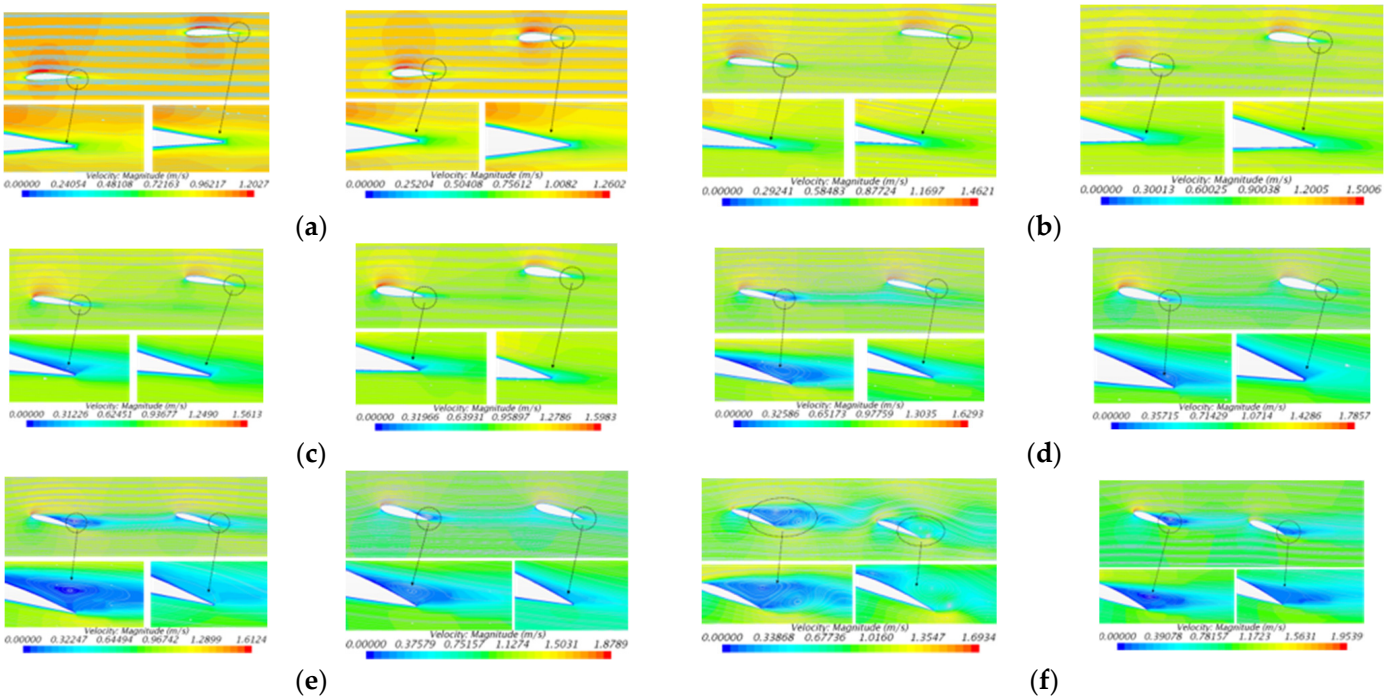

Figure 12. Velocity and streamline distribution in the middle longitudinal section of the wing at different angles of attack: $\alpha = 0°$ (**a**), $\alpha = 6°$ (**b**), $\alpha = 8°$ (**c**), $\alpha = 12°$ (**d**), $\alpha = 15°$ (**e**), $\alpha = 20°$ (**f**) (in each sub-image, **left**: NACA2412; **right**: NACA2418).

Figure 12a–f shows the velocity distribution with streamlines of the longitudinal profiles of airfoil NACA2412 (left) and NACA2418 (right) hydrofoil at the angle of attacks of 0°, 6°, 8°, 12°, 15°, and 20°, respectively. It was found that as the angle of attack increased, the vertical distance between the front and rear hydrofoils in the direction of the heading flow became smaller, which gradually caused the aggravating wake interaction between the front hydrofoil and the rear one. When the angle of attack was 0°, the streamlines around the front and rear hydrofoils were stable and uniform. The wake of the front hydrofoil exerted little impact on the rear hydrofoil. When the angle of attack was 6°, the streamlines near the leading edge of the rear hydrofoil were uneven and tended to concentrate on the upper surface of the leading edge. When the angle of attack was 8°, the front hydrofoil of airfoil NACA2412 began to produce vortices, which were more apparent if the angle of attack was 12°, 15°, or 20°. Moreover, the rear hydrofoil vortices only appeared around the NACA2412 hydrofoil at a higher angle of attack of 20°, which is because the flow velocity through the rear hydrofoil slowed down after flowing through the front one. Benefiting from the proposed rhomboid wing configuration, the separation of the front hydrofoil is delayed until a large angle of attack, and the rear one with greater attached flow would maintain more lifting force, thereby enhancing the performance and motion stability of the AUG.

3.5. Verification of the Numerical Simulation for the Hybrid-Driven AUG without Propeller

In this section, the resistance test of the optimal model (p = 2; θ = 15°; NACA2418) was designed and executed. Due to the limitation of the experimental facilities, the test target was bound to be downscaled. The resistance test of the hybrid-driven AUG scale model with a scale ratio λ = 1:4, as shown in Figure 13, was carried out. In the following paper, the scale model is called the S-AUG for convenience. The effective maximum length of S-AUG *Ls* was 0.5 m. The drag characteristics of the model at different angles of attack under constant inflow were measured and compared with the corresponding CFD data. Figure 14 shows the scheme of the test system in a circular water tank, together with the real test scene in Figure 15. The water surface height was set as 0.4 m, and the distance between the axis of S-AUG and water surface was 0.2 m. With the help of the flow rectifier at the end of the tank, the velocity distribution of the flow in the same intersection plane was nearly uniform. The flow rate was stabilized as 0.4 m/s, which was monitored by an ADV (acoustic Doppler velocimetry) device. The drag of the S-AUG in the flow was detected through a baresthesiometer sensor above the connecting rod, with a precision of 0.001 N. Figure 16 shows the test results of an angle of attack of 0° processed by a smoothing filter. During the experiment, the datum at each angle of attack was measured for a sufficiently long period of time.

Figure 13. The S-AUG model.

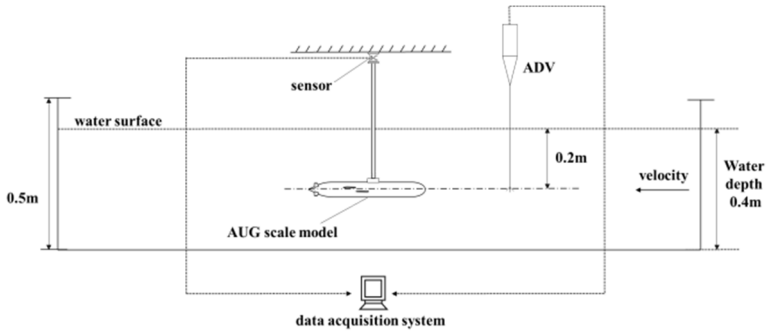

Figure 14. Schematic diagram of the test system.

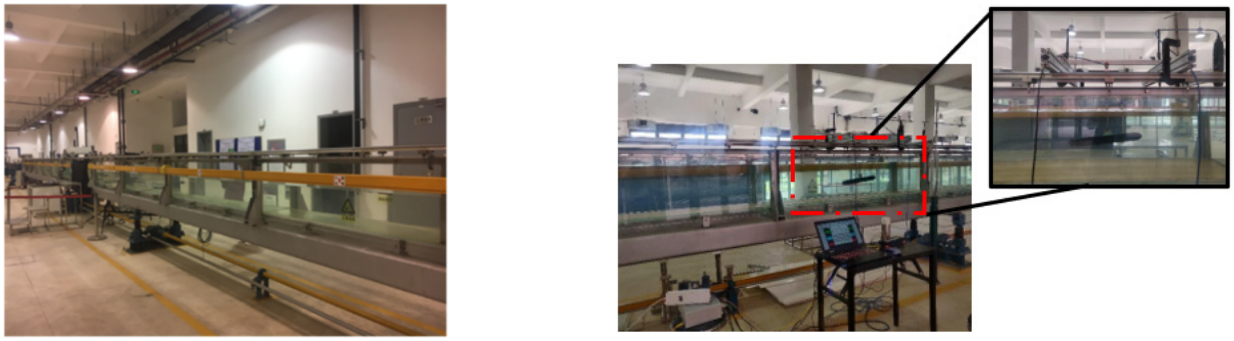

(**a**) (**b**)

Figure 15. Test scene from a whole view (**a**) and a side view (**b**).

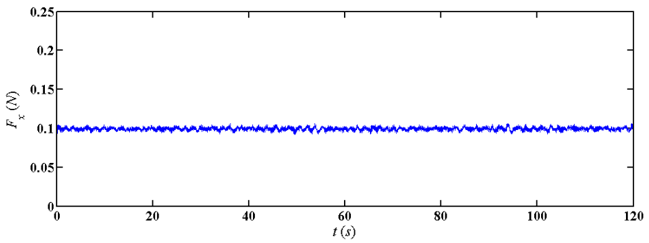

Figure 16. Measurement results after smoothing filtering ($\alpha = 0°$).

According to the main scale parameters of the test tank and S-AUG, a parallel tank of 4.0 m × 0.3 m × 0.8 m was established in the CFD simulation, as shown in Figure 17. The VOF (volume of fluid) method was used to capture the free surface, and the mesh on the free surface was encrypted. The total number of generated grids was 2.8×10^6.

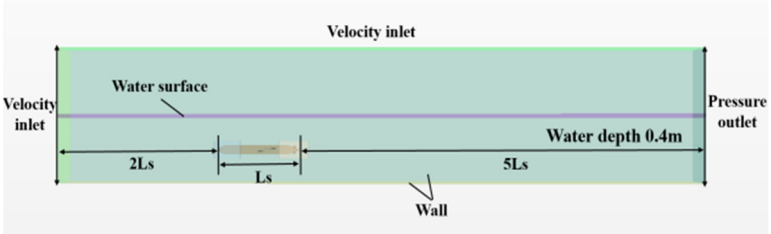

Figure 17. Numerical towing tank with the boundary conditions.

The simulation results were compared with the test results, as shown in Figure 18. The experimental drag values were slightly larger than the CFD simulation results, which may be due to the existence of the angle of attack and cylindrical connecting rod in the test. At

each angle of attack, the errors between the test values and the simulation values were less than 5%, which shows that the simulations had sufficient accuracy.

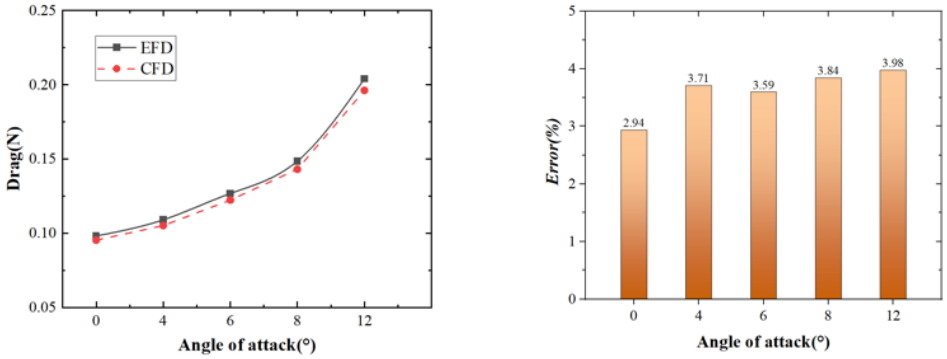

(a) (b)

Figure 18. The experimental and simulation results (**a**) and error assessment (**b**) of S-AUG (V = 0.4 m/s; Error = (EFD − CFD)/CFD × 100%).

4. Self-Propulsion Analysis of the Hybrid-Driven AUG

4.1. Test and Simulation of a Single Propeller

According to the lever principle and the actual size of the tank, the thrust test mechanism shown in Figure 19a was designed. In the test, the propeller Whale715, with a diameter of 0.125 m, was driven by the motor to generate thrust, as shown in Figure 19b,c. The water depth was set as 0.4 m and the inlet velocity was 0.5 m/s. During the test, by controlling the rotation rate of the propeller, the reading of the tensiometer was recorded to obtain the thrust at different rotation rates after conversion.

(a) (b) (c)

Figure 19. The equipment of propeller thrust test, the thrust test bracket (**a**), Whale715 propeller with the electric motor (**b**), and the combination of the test system (**c**).

Related to the test, a series of corresponding simulations were conducted by combining the SM (sliding mesh) method with the SST k-ω turbulence model. The strategy was uniformly adopted in the following paper. The comparison of the simulation and test results in terms of thrust are shown in Figure 20.

According to Figure 20, it can be seen that when the rotation rate was 400~1200 rpm, the calculation results were slightly larger than the experimental values. At a low rotation rate (400 rpm), the calculation error was large, reaching 4.76%, but the errors of all rotation rates were less than 5%. As it turns out, the SM method with the SST k-ω turbulence model is also suitable for the calculation of rotational motion.

4.2. Simulation of 715 CRP

Under the same thrust requirements, the CRP diameter can be smaller than that of the single propeller due to the effects of energy recovering in wake contraction, etc. In this section, the diameter of the Whale 715 single propeller was reduced to 0.9 times of the original one as the front propeller of the CRP, together with the rear propeller diameter 96.43% of the front propeller. The geometric dimension parameters are shown in Table 2.

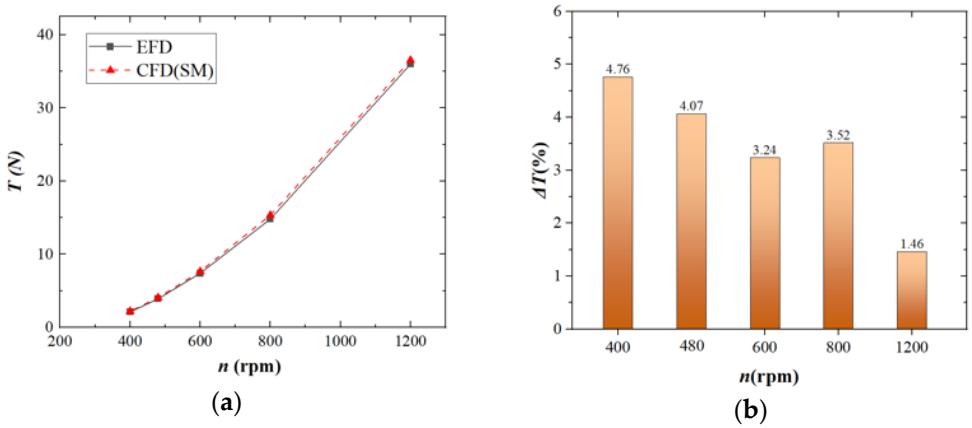

Figure 20. Propeller test and simulation results (**a**) and the error assessment of the simulation results (**b**).

Table 2. The main parameters of the CRP.

Parameter	Front Propeller	Rear Propeller
Diameter	112 mm	108 mm
Direction of rotation	Dextral rotation	Levo rotation
Number of blades	3	3

The simulation of the CRP hydrodynamic performance was carried out in a cylindrical tank, and the whole tank was divided into three parts: the outermost static domain and two rotation domains, as shown in Figure 21a, with the mesh results shown in Figure 21b. The total mesh cell number was 2.1 million. The rotation speeds of both CRP propellers were initially set at the same level of 720 rpm reversely, and the calculation time step was set as 2×10^{-4} s. The prediction of the hydrodynamic performance under different advance coefficients (J = 0.1~1.0) could be realized by changing the inlet velocity of the tank.

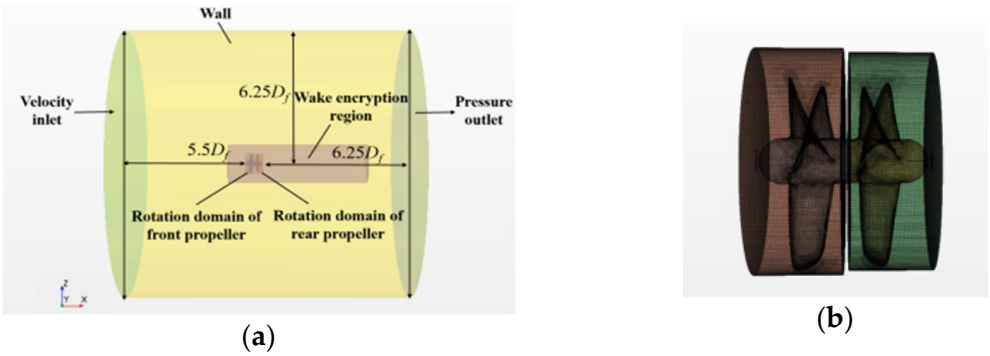

Figure 21. Calculation domain (**a**) and mesh (**b**) of the CRP.

Figure 22 shows the numerical open water performance of the CRP when J is in the range of 0.1~1.0. The results showed that the thrust and torque of the front propeller were greater than that of the rear propeller. With the increase in the advance coefficient, the thrust and torque of the front propeller and the rear propeller both decreased gradually, which was due to the decrease in the angle of attack of the propeller against the flow as the thrust output decreased. In addition, the torque generated by the front propeller and the rear propeller was in opposite directions. The overall torque was maintained between 0 and ~0.025 N-m, which showed excellent behavior during the balance of torque.

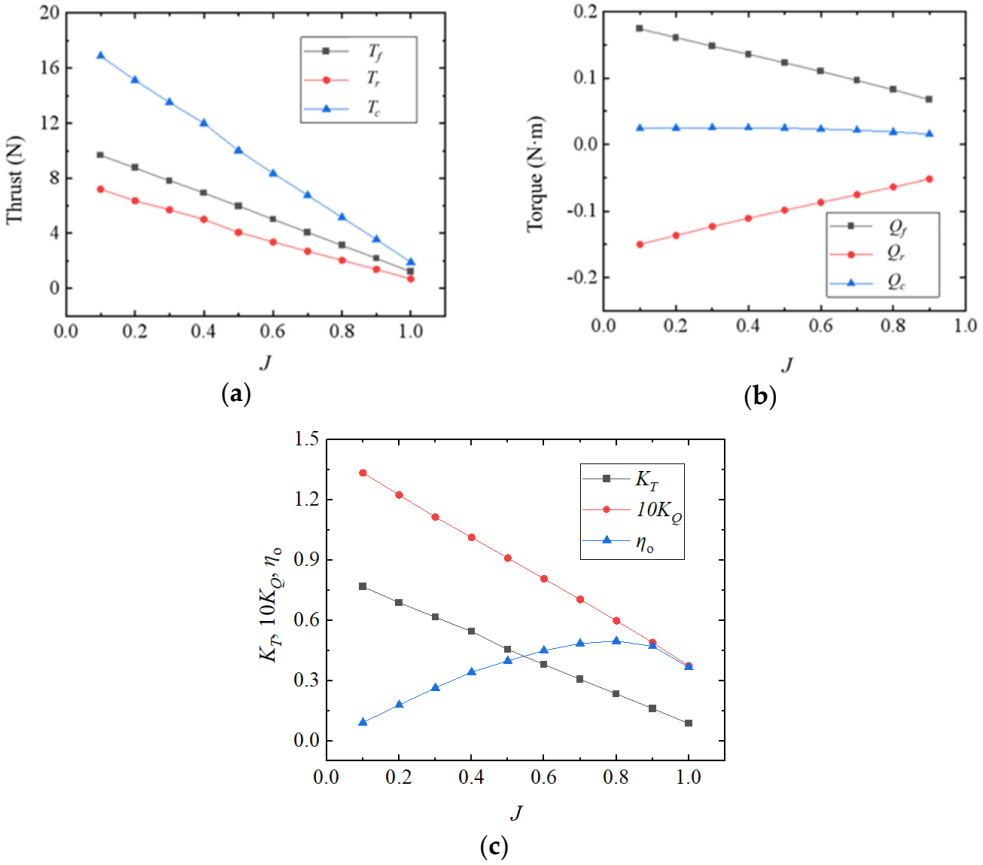

Figure 22. The open water performance of the CRP in terms of the thrust output (**a**), the torque output (**b**), and the dimensionless *K-J* parameters (**c**) (subscript *f*: front propeller; *r*: rear propeller; *c*: counter rotating propeller).

Figure 23 shows the pressure distribution of the CRP surface when J = 0.1, 0.3, 0.5, and 0.7. With the increase in the advance speed coefficient J, the pressure on the pressure surface dropped, while the area of the low-pressure region on the suction surface (mostly concentrated on the leading edge and blade tip) gradually expanded. This resulted in the pressure difference between the suction surface and the pressure surface gradually decreasing with the advance speed coefficient, which is the principal component of the thrust.

Figure 24 shows the wake flow of the CRP under different advance speed coefficients. The CRP produced an obvious wake contraction phenomenon, which was more prominent at a low advance speed. With the increase in the advance speed coefficient, the wake contraction phenomenon gradually weakened, indicating that the influence of the CRP on the nearby fluid was smaller and the wake field was more regular.

4.3. Self-Propulsion Simulation of the Hybrid-Driven AUG with the Single Propeller

The geometry and calculation domain are shown in Figure 25 including the numerical towing tank of self-propulsion simulation and boundary conditions. The towing tank adopted a cylindrical basin with a length of 10 L and a radius of 3 L. The velocity inlet was located 3 L from the bow of the AUG, and the pressure outlet was located 6 L downstream of the stern. We set the volume encryption region and wake encryption region, and the length of the wake region was set as 4 L. The mesh strategy of the AUG hull was the same as that in Section 3. The total number of generated grids was 5.17 million, as shown in Figure 26.

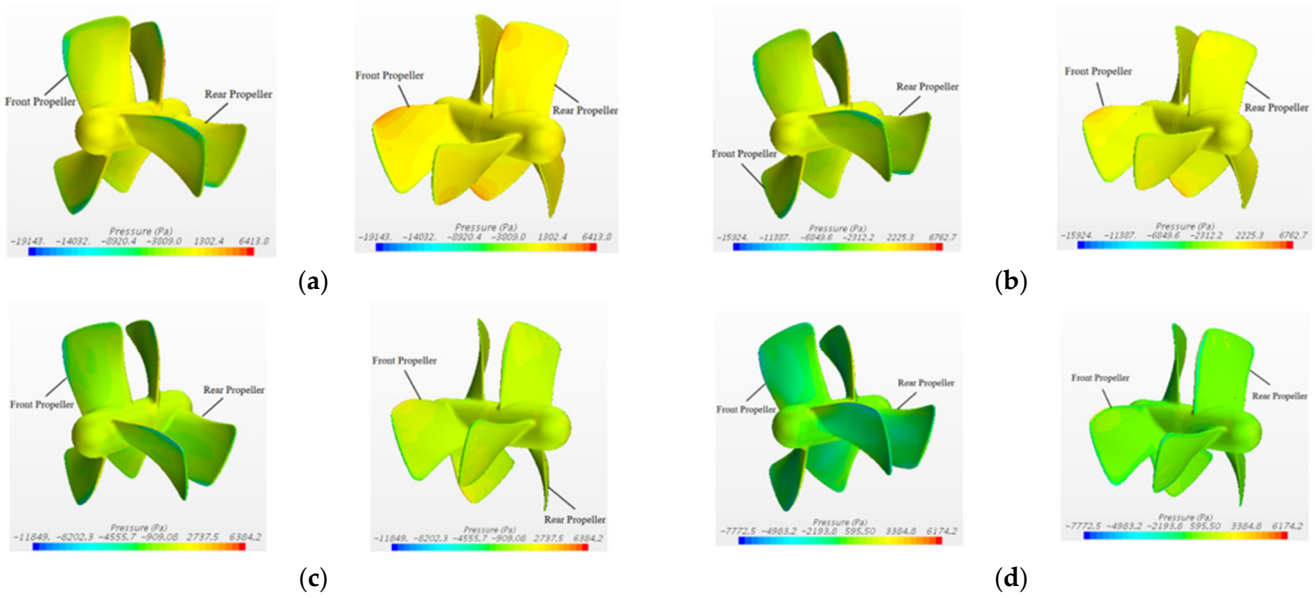

Figure 23. Pressure distribution on the CRP surfaces with different advance coefficients, J = 0.1 (**a**), J = 0.3 (**b**), J = 0.5 (**c**), and J = 0.7 (**d**).

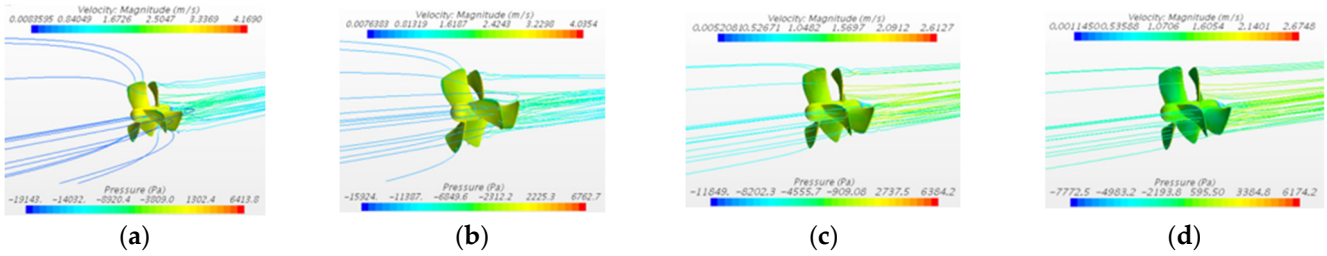

Figure 24. Wake streamline distribution of CRP, J = 0.1 (**a**), J = 0.3 (**b**), J = 0.5 (**c**), and J = 0.7 (**d**).

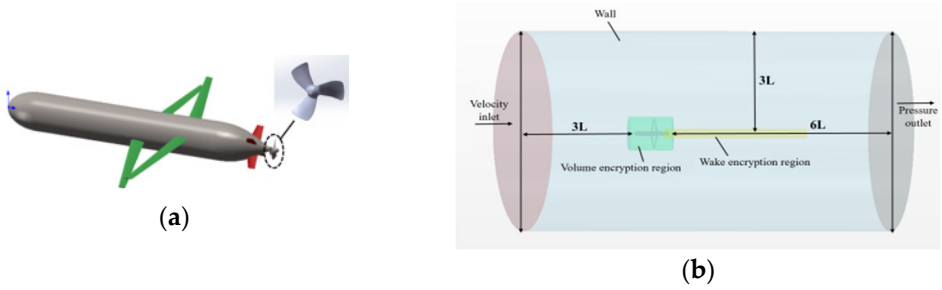

Figure 25. The 3D model (**a**) and the calculation domain (**b**) of the hybrid-driven AUG with the single propeller.

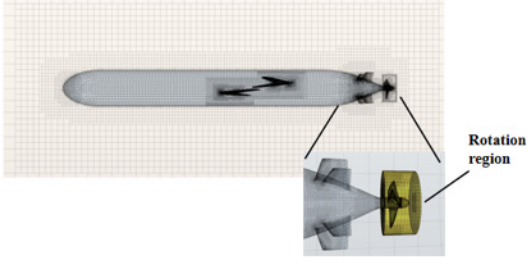

Figure 26. Mesh of the hybrid-driven AUG with the single propeller.

The propeller rotation rates were initially set as 720 rpm and 900 rpm. The designed speed of the hybrid-driven AUG was 1.4 m/s. With a given inflow velocity, the propeller was set to rotate at different rotation rates to monitor the resistance of the bare AUG hull and the propeller thrust, as shown in Figure 27.

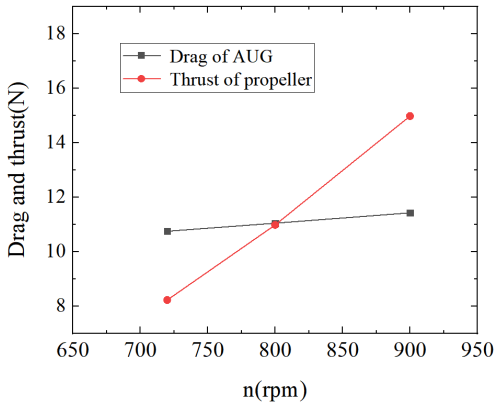

Figure 27. Self-propulsion results of the hybrid-driven AUG with the single propeller.

As can be seen, with the increase in the rotation rate, the thrust of the propeller increased significantly at the given speed of 1.4 m/s, while the resistance of the hybrid-driven AUG increased relatively slowly. It was estimated from the intersection point of the curves in Figure 27 that the propeller rotation speed for self-navigation was 800 rpm when the thrust and the resistance were close to equilibrium and the AUG reached a stable speed. Table 3 shows that when the propeller was simulated at 800 rpm, the propeller thrust was 10.98 N and the resistance of the hybrid-driven AUG was 11.044 N, with a difference of 0.6%. This was considered that the hybrid-driven AUG had reached the self-propulsion state.

Table 3. Calculation results of the self-propulsion state for the hybrid-driven AUG with the single propeller.

V (m/s)	n (rpm)	F_D (N)	T (N)	Q (N-m)
1.4	800	11.044	10.980	0.247

Furthermore, the flow field distribution of the hybrid-driven AUG with the single propeller at the same inlet velocity and different rotation rates, as shown in Figure 28. The velocity cloud diagram of the longitudinal profile in the stern of AUG is shown in the left column, and the velocity cloud diagram of the flow field at 0.085D behind the single propeller disk is shown in the right column. It was found that the wake of the propeller hub and the high-speed region of the wake both transferred to the distance, and the tip of the propeller stretched two tip vortices as the propeller rotated, which gradually disappeared following the wake.

4.4. Self-Propulsion Simulation of the Hybrid-Driven AUG with the CRP

It should be noted that the torque of the propeller was 0.247 N-m. Due to the small transverse size of the AUG (the maximum diameter of the parallel body was 0.22 m), it cannot balance the torque generated by the single propeller through its restoring moment for rolling. In order to solve the above problems to balance the overall torque of the hybrid-driven AUG and ensure the stability of its sailing attitude, the propulsion form of the contra-rotating propeller was adopted.

The 3D diagram of the hybrid-driven AUG with the CRP is shown in Figure 29. The mesh strategy and calculation domain were the same as those described in Section 4.3.

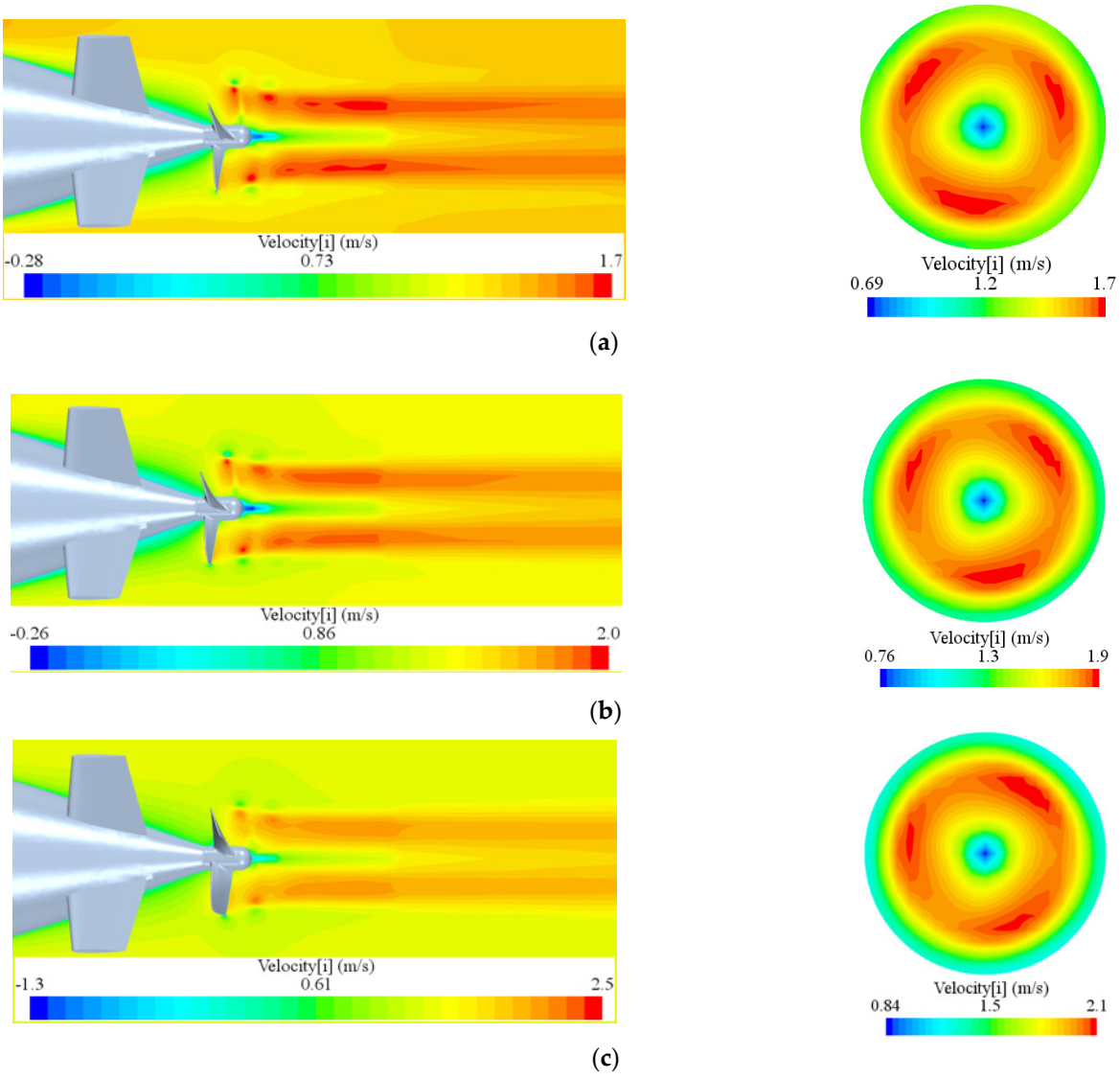

Figure 28. Velocity distribution of the hybrid-driven AUG with the single propeller with propeller rotation speeds of 720 rpm (**a**), 800 rpm (**b**), and 900 rpm (**c**).

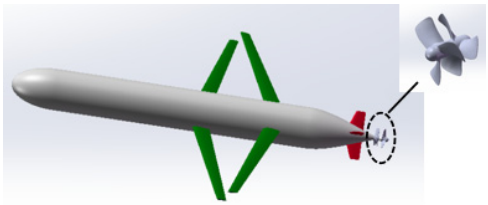

Figure 29. Model of the AUG with the CRP.

The design speed was also 1.4 m/s. Under the given coming flow speed, the propeller was set to rotate at different rotation rates (720 rpm, 800 rpm, 900 rpm), and the AUG resistance value D and propeller thrust value T were monitored, as shown in Figure 30. It was estimated that the thrust and resistance were close to equilibrium and the CRP revolution was 780 rpm during self-propulsion at the designed speed. Consequently, at the designed speed of 1.4 m/s, the resulting revolutions of the AUG with CRP would be less than 800 rpm, which is comparable to that of the AUG with the single propeller in the above section.

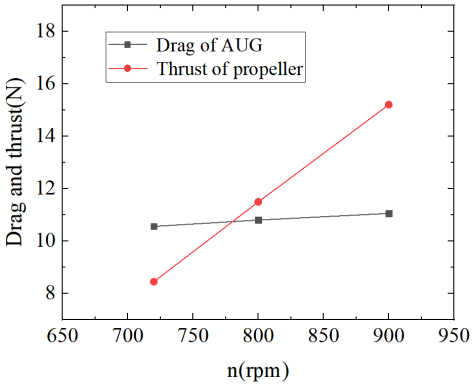

Figure 30. Self-propulsion simulation results of the AUG with the CRP.

A numerical self-propulsion simulation of the AUG equipped with the CRP at 780 rpm was conducted and the results are shown in Table 4. The thrust was 10.68 N, the AUG resistance was 10.73 N, the difference between the thrust and resistance was 0.466%, and the overall torque of the CRP was 0.019 N-m, obviously smaller than that with a single propeller at 92.31%.

Table 4. Calculation results of the self-propulsion state of the maneuverable AUG with the CRP.

V (m/s)	n (rpm)	F_D (N)	Propeller Thrust (N)			Propeller Torque (N-m)		
			T_f	T_a	T	Q_f	Q_a	Q
1.4	780	10.73	6.11	4.57	10.68	0.129	−0.110	0.019

The flow field distributions of the hybrid-driven AUG with the CRP at the same inlet velocity and different rotation rates are shown in Figure 31. It can be found that when the propeller rotated, both the wake of the propeller hub and the high-speed region of the wake were transmitted to the far downstream, and the tip of the propeller stretched two tip vortices, which gradually disappeared along the wake direction. Compared with Figure 28, from the perspective of wake distribution, the wake contraction degree of the propeller was more obvious. By absorbing the energy from the front propeller, the average speed of the wake of the CRP was less than that of the single propeller.

4.5. The Self-Propulsion Comparation of AUGs with Different Hull Lines Matched with CRP

To further explore the influence of different hull lines on the self-propulsion performance, this paper also conducted self-propulsion simulations for the hybrid-driven AUG with the hull lines of (p = 2; θ = 25°; NACA2418) and (p = 3; θ = 25°; NACA2418), calculating the self-propulsion factor, respectively. The self-propulsion simulation results of two hybrid-driven AUGs are shown in Figure 32. At the designed speed of 1.4 m/s, the rotation speed of the hybrid-driven AUG with the hull line (p = 2; θ = 25°; NACA2418) was 755 rpm in self-propulsion state, and the rotation speed was 760 rpm when the hull line was (p = 3; θ = 25°; NACA2418).

A numerical simulation comparation at the self-propulsion point of the three hybrid-driven AUGs equipped with the CRP was conducted and the results are shown in Table 5. The self-propulsion factors were calculated by Equations (16)–(20). From the perspective of the torque for the AUG, the overall torque of the hybrid-driven AUG with the hull line of (p = 2; θ = 25°) matched with the CRP would be reduced by 91.9% compared with that of the same AUG shape matched with a single propeller. Additionally, the overall torque of the hybrid-driven AUG with the hull line of (p = 3; θ = 25°) matched with the CRP would be reduced by 93.9% compared with that of the same AUG shape matched with a single propeller.

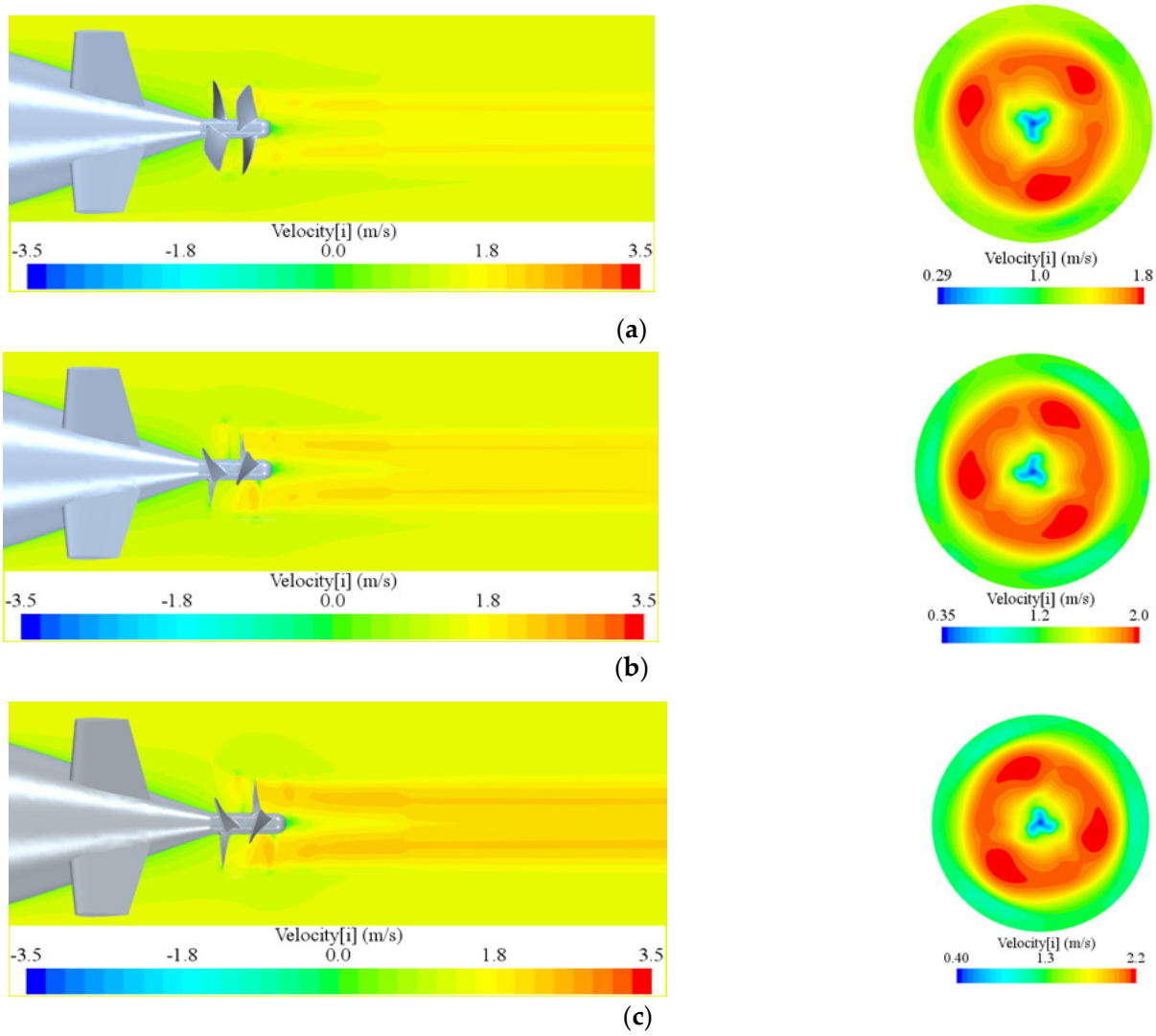

Figure 31. Velocity distribution of the hybrid-driven AUG with the CRP at rotation speeds of 720 rpm (**a**), 800 rpm (**b**), and 900 rpm (**c**) including the sideview of the wake and the axial velocity plane $0.085D_a$ downstream of the rear propeller disk.

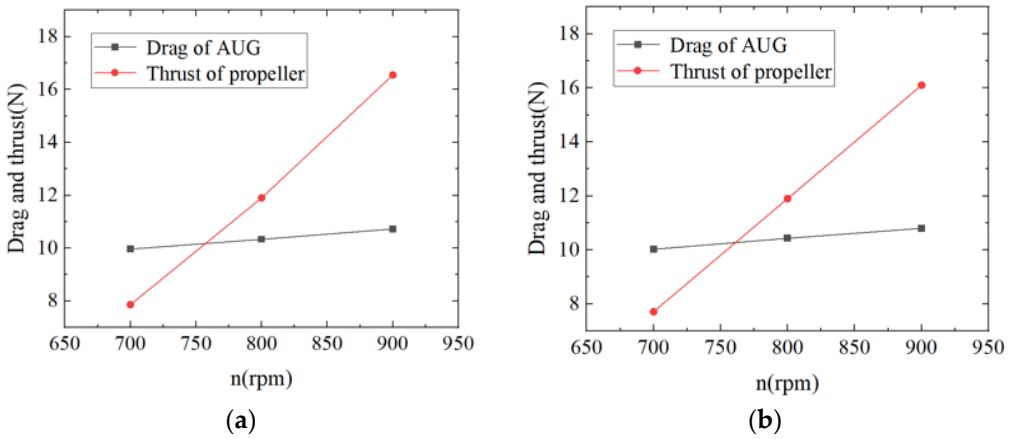

Figure 32. The self-propulsion simulation results of the hybrid-driven AUGs with different hull lines, (p = 2; θ = 25°; NACA2418) (**a**) and (p = 3; θ = 25°; NACA2418) (**b**).

Table 5. The calculation results of the self-propulsion factor of the different hull line AUGs with the CRP.

Hull Line	V (m/s)	V_A (m/s)	n (rpm)	J	F_D (N)	T_B (N)	Q_0 (N-m)	Q_B (N-m)	P_E (W)	η_R	η_0	η_H	P_B (W)
$p = 2; \theta = 15°$	1.4	1.040	780	0.7143	10.73	10.68	0.205	0.239	15.022	0.860	0.48525	1.350	26.664
$p = 2; \theta = 25°$	1.4	0.995	755	0.7060	10.14	10.01	0.194	0.220	14.196	0.882	0.48509	1.425	23.284
$p = 3; \theta = 25°$	1.4	0.999	760	0.7040	10.20	10.00	0.198	0.215	14.280	0.921	0.48505	1.429	22.369

It can be seen from Table 5, that the type of ($p = 3; \theta = 25°$) had a strong propulsion performance by comparing the propeller rotation speed and the brake horsepower. According to the power relationship, the motor horsepower P_S emitted by this type of hybrid-driven AUG was estimated to be 23.3 W, and Equation (23) was used to calculate the current when the rated voltage of the motor was 48 V. The current of the motor was 0.485 A during the running time. The P_S of the other two AUGs, ($p = 2; \theta = 15°$) and ($p = 2; \theta = 25°$), were 27.8 W and 24.3 W, respectively, under the consideration of a shaft transmission efficiency of 0.96 from the values of P_B, and the currents of the motor were 0.579 A and 0.506 A, respectively.

$$P_s = UI \tag{23}$$

where U is the voltage and I represents the current.

The lithium battery with the capacity and volume considered is shown in Figure 33. The capacity of the battery was 25 Ah with the volume of 250 mm × 145 mm × 75 mm, of which the weight was 2 kg. This can meet the continuous operation of the motor under normal operation for 43.1 h, 49.4 h, and 51.5 h for the hybrid-driven AUGs with the shape of ($p = 2; \theta = 15°$; NACA2418), ($p = 2; \theta = 25°$; NACA2418), and ($p = 3; \theta = 25°$; NACA2418) as discussed above, respectively. Meanwhile, the battery can actually be placed in the AUG.

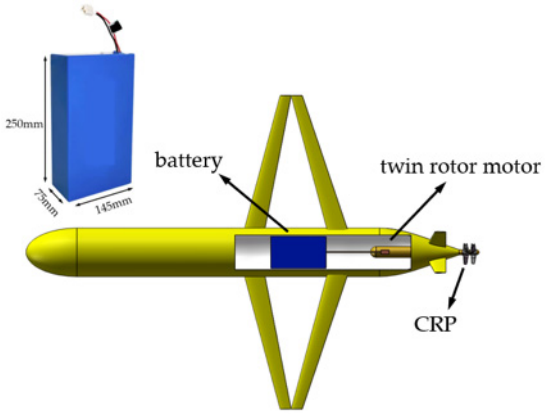

Figure 33. Concept chart of the battery and the propulsion system.

5. Conclusions

This paper designed and analyzed a hybrid-driven autonomous underwater glider, through CFD numerical simulations and experiments, on the basis of an AUG with a rhomboid hydrofoil configuration originating from an existing AUG. Following the optimization of the hull geometry, the appropriate foil type was selected in terms of the gliding motion. With the optimized hydrodynamic shape, the self-propulsion simulation analysis was carried out combined with both a single propeller and the relative contra-rotating propeller. The main research results are listed as follows.

1. In this paper, numerical simulations of the rhomboid wings with different hydrodynamic shapes were conducted under the condition of straight-line motion and oblique motions (i.e., the gliding motion). Comparing the hydrodynamic coefficients,

the hydrodynamic shape of the rhomboid wing was optimized. Through comprehensive comparison, the AUG with a hull line shape (p = 2; θ = 15°) and hydrofoil NACA2418 presented the best performance, where the lift–drag ratio increased by 22.5% compared with the initial model at an 8° angle of attack for the designed working condition.

2. The drag tests and numerical simulations of the scale model of the hybrid-driven AUG with the optimized hydrodynamic shape were carried out without the propeller. Compared with the experimental results, the reliability of the numerical method was verified.
3. The open water performance tests and corresponding simulations of the Whale715 propeller were conducted to verify the CFD simulation results in this paper. The results showed that the SST k-ω turbulence model could accurately predict the propeller hydrodynamic performance.
4. Based on the open water simulations and tests for the Whale715 single propeller and its relative contra-rotating propeller, the self-propulsion performance of the hybrid-driven AUG with the single propeller and CRP was analyzed, respectively, at the designed speed. The results showed that the overall torque of the hybrid-driven AUG with the CRP was notably reduced by 92.3% compared with that of the AUG with a single propeller. Due to the greater thrust output, the hybrid-driven AUG with the CRP could reach the self-propulsion point at a lower propeller rotation speed. In addition, the self-propulsion performance with the CRP for the AUGs with various hull lines was compared, which indicated that the hybrid-driven AUG under the optimization design mainly based on the premise of the gliding motion might not show an excellent behavior during the self-propulsion motion with the straight-line route.

The propeller applied in this paper possessed a wide blade tip, suitable for combining with the duct, which is worth further optimization in the future. Moreover, due to the addition of propellers, the upstream area of the hybrid-driven AUG magnifies, and the resistance and the power consumption in gliding motion significantly increase, which is a vital factor restricting the development and application of the hybrid-driven AUG. Currently, some researchers have proposed a solution of folding propeller blades during the gliding motion, which might be a research orientation in the future.

Author Contributions: Conceptualization, C.-W.C.; methodology, Z.-Y.Z.; validation, X.-P.C. and X.-J.Z.; formal analysis, X.-J.Z. and X.-P.C.; investigation, Z.-Y.Z. and X.-P.C.; data curation, X.-J.Z. and X.-P.C.; writing—original draft preparation, Z.-Y.Z., X.-P.C. and C.-W.C.; writing—review and editing, C.-W.C., Z.-Y.Z. and X.-P.C.; supervision, C.-W.C.; funding acquisition, C.-W.C. All authors have read and agreed to the published version of the manuscript.

Funding: This research was supported by Ocean College of Zhejiang University, and funded by TXC (Ningbo) Co., Ltd. (Item NO.529203-I22004).

Institutional Review Board Statement: Not applicable.

Informed Consent Statement: Not applicable.

Data Availability Statement: Not applicable.

Conflicts of Interest: The authors declare no conflict of interest.

Nomenclature

Symbol	Parameter	Unit	Symbol	Parameter	Unit
J	Advance speed coefficient	[-]	L	Effective maximum length of AUG	[m]
K_T	Thrust coefficient	[-]	Ls	Effective maximum length of S-AUG	[m]
K_Q	Torque coefficient	[-]	D_h	Maximum diameter of the hull	[m]
T	Thrust of propeller	[N]	B	Wingspan of the hydrofoil	[m]
Q	Torque of propeller	[N-m]	a	Length of the bow	[m]
T_B	Propeller thrust under the self-propulsion condition	[N]	b	Length of AUG parallel middle body	[m]
Q_0	Propeller torque in open water test	[N-m]	c	Length of the stern	[m]
Q_B	Propeller torque under the self-propulsion condition	[N-m]	C_t	Chord length of the hydrofoil tip	[m]
η_o	Propulsion efficiency of propeller in the open water condition	[-]	C_r	Chord length of the hydrofoil root	[m]
η_R	Shaft transmission efficiency	[-]	p	Sharpness factor	[-]
η_H	Hull efficiency	[-]	θ	Angle of run	[°]
P_B	Brake horsepower	[W]	α	Angle of attack	[°]
P_E	Effective horsepower	[W]	S	Wet surface area of the hydrofoil	[m^2]
P_S	Motor horsepower	[W]	$S\text{-}AUG$	Scale model of AUG	[-]
D	Propeller diameter	[m]	C_D	Drag coefficient	[-]
D_f	Diameter of front propeller	[m]	C_L	Lift coefficient	[-]
D_a	Diameter of rear propeller	[m]	F_D	Drag of AUG	[N]
n	Rotation speed of propeller	[rps]	F_L	Lift of AUG	[N]
V_A	Advance speed of propeller	[m/s]	$\bigtriangledown$	Displacement of AUG	[m^3]
T_f	Thrust of front propeller	[N]	V	Navigation speed of AUG	[m/s]
T_a	Thrust of rear propeller	[N]	ρ	Water density	[kg/m^3]
T_c	Thrust of CRP	[N]	K_{Tf}	Thrust coefficient of front propeller	[-]
Q_f	Torque of front propeller	[N-m]	K_{Ta}	Thrust coefficient of rear propeller	[-]
Q_a	Torque of rear propeller	[N-m]	K_{Qf}	Torque coefficient of front propeller	[-]
Q_c	Torque of CRP	[N-m]	K_{Qa}	Torque coefficient of rear propeller	[-]
U	Voltage	[V]	QPC	Quasi-propulsive coefficient	[-]
I	Current	[A]	$Pressure$	Pressure distribution of blade surface	[Pa]

References

1. Rudnick, D.L.; Davis, R.E.; Eriksen, C.C.; Fratantoni, D.M.; Perry, M.J. Underwater Glider for Ocean Research. *Mar. Technol. Soc. J.* **2004**, *38*, 73–84. [CrossRef]
2. Liu, Y.J.; Liu, J.; Pan, G.; Huang, Q.G.; Guo, L.M. Dynamic Analysis of an Autonomous Underwater Glider with Single- and Two-Stage Vibration Isolators. *J. Mar. Sci. Eng.* **2022**, *10*, 162. [CrossRef]
3. Li, Y.C.; Ma, Z. Numerical investigation on novel conceptual design of hybrid-driven autono-mous underwater glider with active twin flapping foils. *Ocean Eng.* **2020**, *214*, 107867. [CrossRef]
4. Li, Y.C.; Hu, J.X.; Zhao, Q.Z.; Pan, Z.Y.; Ma, Z. Hydrodynamic Performance of Autonomous Underwater Gliders with Active Twin Undulatory Wings of Different Aspect Ratios. *J. Mar. Sci. Eng.* **2020**, *8*, 476. [CrossRef]
5. Shen, X.R.; Wang, Y.H.; Yang, S.Q.; Liang, Y.; Li, H.Z. Development of underwater gliders: An overview and prospect. *J. Unmanned Undersea Syst.* **2018**, *26*, 89–106.
6. Ebata, S.; Yasuda, T.; Minagawa, H.; Miyamoto, Y.; Satofuka, N. A Study of Cross-Sectional Shape of Wing for Underwater Glider at Low Reynolds Number Region. *Trans. Jpn. Soc. Mech. Eng.* **2013**, *79*, 1886–1899. [CrossRef]
7. Singh, Y.; Bhattacharyya, S.K.; Idichandy, V.G. CFD Approach to Modelling, Hydrodynamic Analysis and Motion Characteristics of a Laboratory Underwater Glider with Experimental Results. *J. Ocean Eng. Sci.* **2017**, *2*, 90–119. [CrossRef]
8. Chen, C.W.; Feng, Z.; Liang, X. Hydrodynamic Analysis of Underwater Glider with Diamond Wing in Unsteady and Nonuniform Flow Field. *J. Mar. Sci. Technol.* **2018**, *26*, 787–802.
9. Shankar, R.V.S.; Vijayakumar, R. Numerical Study of the Effect of Wing Position on Autonomous Underwater Glider. *Def. Sci. J.* **2020**, *70*, 214–220. [CrossRef]
10. Jay, A. The potential for Autonomous Underwater Gliders in large lake research. *J. Great Lakes Res.* **2013**, *39*, 8–13.
11. Paul, M.K.; Tom, H.; Joel, H. Autonomous underwater glider observations in southern Lake Ontario and Niagara River plume. *Aquat. Ecosyst. Health Manag.* **2022**, *25*, 102–113.
12. Jenkins, S.A.; Humphreys, D.E.; Sherman, J. *Underwater Glider System Study*; Scripps Institution of Oceanography Technical Report; Office of Naval Research: Arlington, VA, USA, 2003.

13. Madureira, L.; Sousa, A.; Sousa, J.; Gonçalves, G. Low Cost Autonomous Underwater Vehicles for New Concepts of Coastal Field Studies. *J. Coast. Res.* **2009**, *2*, 59–62.
14. Bachmayer, R.; Leonard, N.E.; Gravery, J.; Fiorelli, E.; Paley, D. Underwater gliders: Recent developments and future applications. In Proceedings of the IEEE Proceeding of International Symposium on Underwater Technology, Taipei, Taiwan, 20 May 2004.
15. Griffiths, G.; Jones, C.P.; Ferguson, J.; Bose, N. Undersea glider. *J. Ocean. Technol.* **2007**, *2*, 64–75.
16. Yamamoto, I. Research and development of past, present, and future AUV technologies. *Under-Water Technol.* **2006**, *69*, 28–29.
17. Wood, S.; Allen, T.; Kuhn, S. *Autonomous Underwater Vehicle: Powered Glider*; Technical Report; Florida Institute of Technology: Melbourne, FL, USA, 2007.
18. Wood, S.; Allen, T.; Kuhn, S.; Caldwell, J. The development of an autonomous underwater powered glider for deep-sea biological, chemical and physical oceanography. In Proceedings of the OCEANS 2007—Europe, Aberdeen, UK, 18–21 June 2007; pp. 1–6.
19. Jones, C.; Allsup, B.; Webb, D. Glider Expanding the Capabilities. *Mar. Technol. Soc.* **2011**, 58.
20. Liu, F.; Wang, Y.H.; Wang, S.X. Development of the Hybrid Underwater Glider Petrel-II. *Sea Technol.* **2014**, *55*, 51–54.
21. Nathan, C.; Pablo, M.C. Submarine propeller computations and application to self-propulsion of DARPA Sub-off. *Ocean Eng.* **2013**, *60*, 68–80.
22. Rattanasiri, P.; Wilson, P.A.; Phillips, A.B. Numerical investigation of a pair of self-propelled AUVs operating in tandem. *Ocean Eng.* **2015**, *100*, 126–137. [CrossRef]
23. Zhang, R.C.; Dong, X.J.; Wang, Z.; Huang, Y.; Yu, J.C. Numerical design and validation of propeller for long-range AUV. *Shipbuild. China* **2019**, *60*, 147–159.
24. Liu, J.X.; Wang, M.; Yu, F.; Gao, S.; Yan, T.H.; He, B. Numerical study on the hull–propeller inter-action of autonomous underwater vehicle. *Ocean Eng.* **2023**, *271*, 113777. [CrossRef]
25. Huang, Y.S.; Dong, X.Q. Design of wake-adapted contra-rotating propellers for high-speed underwater vehicles. *Appl. Ocean. Res.* **2019**, *2*, 91–97. [CrossRef]
26. Kingan, M.J.; Parry, A.B. Acoustic theory of the many-bladed contra-rotating propeller: The effects of sweep on noise enhancement and reduction. *J. Sound Vib.* **2020**, *3*, 468–472. [CrossRef]
27. Wang, Z.; Xiong, Y. Effect of Time Step Size and Turbulence Model on the Open Water Hydrodynamic Performance Prediction of Contra-Rotating Propellers. *China Ocean Eng.* **2013**, *27*, 193–204. [CrossRef]
28. Wang, Z.Z.; Xiong, Y.; Qi, W.J. Numerical prediction of contra-rotating propellers' open water performance. *J. Huazhong Univ. Ence. Technol.* **2012**, *40*, 77–80+88.
29. Hu, J.; Wang, Y.Z.; Zhang, W.P.; Chang, X.; Zhao, W. Tip vortex prediction for contra-rotating propeller using large eddy simulation. *Ocean Eng.* **2019**, *194*, 106410.1–106410.17. [CrossRef]
30. Paik, K.J.; Hwang, S.; Jung, J.; Lee, T.; Lee, T.T.; Ahn, H.; Van, S.H. Investigation on the wake evolution of contra-rotating propeller using RANS computation and SPIV measurement. *Int. J. Nav. Archit. Ocean Eng.* **2015**, *7*, 595–609. [CrossRef]
31. He, D.; Wan, D.; Yu, X. Numerical Investigations of Open-Water Performance of Contra-Rotating Propellers. In Proceedings of the 27th International Ocean and Polar Engineering Conference, San Francisco, CA, USA, 25–30 June 2017.
32. Tang, J.P. *ANSYS FLUNET 16.0 Learning Manual*; People's Posts and Telecommunications Press: Jiangsu, China, 2016; pp. 14–37.
33. Wang, F.J. *Principle and Application of CFD Software for Computational Fluid Dynamics Analysis*; Qsinghua University Press: Beijing, China, 2004; pp. 12–18.
34. Zhou, L.D. Research Progress and Application in Ship and Ocean Engineering Computer Fluid Dynamics. *Acta Aerodyn. Amica Sin.* **1998**, *1*, 122–131.
35. Sun, C.; Song, B.; Peng, W. Parametric Geometric Model and Shape Optimization of an Underwater Glider with Blended-wing-body. *Int. J. Nav. Archit. Ocean Eng.* **2015**, *7*, 995–1006. [CrossRef]
36. Divsalar, K.; Shafaghat, R.; Farhadi, M.; Alamian, R. Numerical Simulation of Hydrodynamic Properties of Alex Type Gliders. *Int. J. Eng.* **2020**, *33*, 1387–1396.
37. Musa, O.; Xiong, C.; Zhou, C.; Gong, L. Assessment of the Modified Rotation/Curvature Correction SST Turbulence Model for Simulating Swirling Reacting Unsteady Flows in a Solid-fuel Ramjet Engine. *Acta Astronaut.* **2016**, *129*, 241–252. [CrossRef]
38. Sheng, Z.B.; Liu, Y.Z. *Ship Principle*; Shanghai Jiaotong University Press: Shanghai, China, 2004; pp. 17–48.
39. Ghassemi, H.; Taherinasab, M. Numerical calculations of the hydrodynamic performance of the contra-rotating propeller (CRP) for high speed vehicle. *Pol. Marit. Res.* **2013**, *20*, 13–20. [CrossRef]
40. Yu, J.C.; Zhang, A.Q.; Jin, W.M.; Chen, Q.; Tian, Y.; Liu, C.J. Development and Experiments of the Sea-Wing Underwater Glider. *China Ocean Eng.* **2011**, *25*, 721–736. [CrossRef]
41. Bertram, V. *Practical Ship Hydrodynamics*; Elsvier: Amsterdam, The Netherlands, 2012; p. 3.
42. Adapco. *STAR-CCM+ Theory Guide*; CD-ADAPCO: Melville, NY, USA, 2021.
43. Myring, D.F. A Theoretical Study of Body Drag in Subcritical Axisymmetric Flow. *Aeronaut. Quartely* **1976**, *27*, 186–194. [CrossRef]